Manifold Representations of Neural Data

May 15, 2025

Arnaud Lamy

***Abstract*—Neuroscience is an exciting field which has captivated the interest of this author. The field is particularly inviting for algorithmic researchers for a number of reasons, such as the recent introduction of many large-scale neural datasets (owing to fantastic improvements in neural implant technology), the strong role of intuition in understanding the data, and the incredible real-world technologies that this data analysis may support, such as high-quality brain-computer interfaces and neural micro-stimulation systems. A central tenet of systems neuroscience is that neural data exhibits a lot of structure, or equivalently that the firing patterns of neurons strongly covary. From this central tenet (and from empirical observations and intuitions) emerges the hypothesis that neural data is much lower-dimensional than the space in which it resides. Then, if neural data is low-dimensional, why constrict it to residing on a linear subspace? Indeed, many neuroscientists hypothesize that neural data resides on a lower-dimensional manifold! This project is guided by a loose goal to explore this claim through visualizations and scree plots while taking the opportunity to explore the space of algorithmic neuroscience and to learn new data science techniques. On the one hand, this write-up seeks to describe and discuss the project's computations which explore the veracity of neuroscience's manifold hypothesis, and on the other hand to highlight some of the author's favorite ideas in systems neuroscience and some of the algorithms that the author learned about.**

I. Introduction

Neural data can be overwhelmingly high-dimensional. Indeed, the human brain is filled with about 86 billion neurons, each of which produces a time-signal according to its firing pattern. It is hypothesized that neural data is highly structured because neuronal signal strongly covary, and capturing this underlying structure explicitly supports the emerging technologies of brain-computer interfaces and neural micro-stimulation systems. Brain-computer interfaces (BCIs) are physical systems which combine neural implants with smart computing to record and interpret neural signals in real-time. BCIs differ in their intended functionality and in the type of neural implants used (e.g. invasive vs non-invasive implants), but a common goal for the field is effective neuroprosthetics – the control of prosthetic limbs through a BCI. Neural micro-stimulation systems consider a converse problem: using knowledge of neuron firing patterns, can you deliver small and highly-controlled electric stimulation to targeted neurons to induce some desired physiological alteration. For example, can you return somatosensory feedback from prosthetic limbs directly to the user's central nervous system? Otherwise, microstimulation to the visual cortex has been shown to induce short flashes of light, and some researchers have performed experiments to test whether microstimulation in the motor cortex can inhibit the success of specific motor tasks [15].

One experiment involves prompting a monkey to control a cursor using a BCI. The task of generating an effective control system for the monkey is (fascinatingly!) two-sided: the monkey learns to use the provided BCI, while the researchers use the resulting neural data to iterate over the BCI to design a more effective system. One method for this task [6] involves using a fixed decoder (a cursor velocity Kalman filter) in conjunction with a *manifold-based stabilizer*. The researchers aim to reduce the effect of recording instabilities by leveraging an assumption that the recorded neural population activity "reflects a stable underlying representation of movement intent that lies within the neural manifold". Specifically, they split the data in time into a number of trials, and for each trial they use factor analysis to relate the neural signal to a smaller number of latent variables corresponding to a lower-dimensional linear subspace. Then, they relate the low-dimensional linear subspaces across trials by applying an orthogonal matrix to overlay them. This is elaborated on in section III. According to the paper, this real-time manifold-based stabilizer is successful in increasing the performance of the monkey for the BCI task.

Hopefully, these examples justify the importance of understanding neural data. Now, we aim to communicate some of the intuitions which guide neuroscience's manifold hypothesis:

1) **Millions of neurons drive the activity of hundreds of muscles.** There's a dimensional mismatch between the number of neurons and the degrees of freedom in the output of the brain. This might be best highlighted for motor systems, wherein the motor cortex contains millions of neurons to drive a much smaller number of muscles. The main dataset considered in this paper corresponds

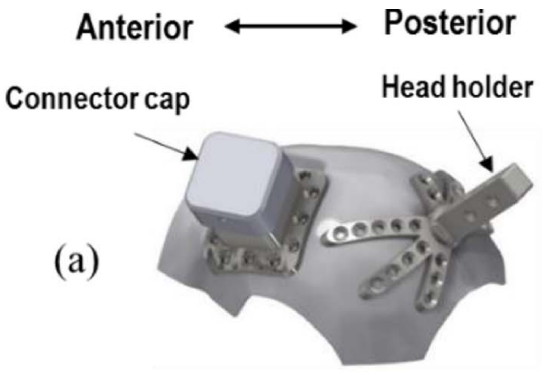

Fig. 1: This depicts the positions of the connector cap and head holder on the skull for the mc-1 dataset. The image and description are taken from [7]

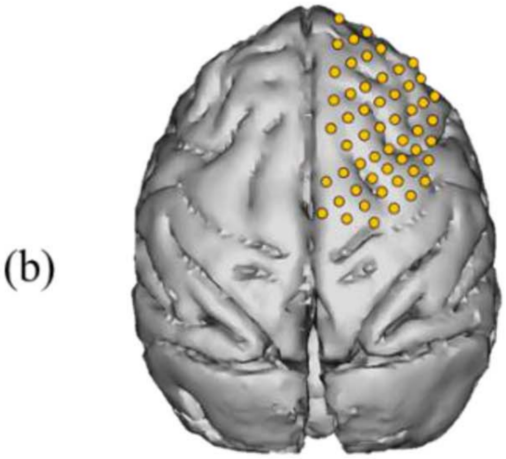

Fig. 2: This depicts the ECoG electrodes implanted subdurally in the right hemisphere of the brain covering from the primary motor cortex to the frontal cortex for the mc-1 dataset. The image and the description are taken from [7]

to a electrocorticographical (ECoG) data from the motor cortex while a monkey performs a task involving both hands, and the data appears to be low-dimensional. The dimensional mismatch guides us to the hypothesis that while neural data exists in a high-dimensional space, it should reside on a lower-dimensional object.

2) **Neural systems may be robust to neuron failure.** It seems that the misfiring of a relevant neuron may not impede the success of a given task. In one paper [15], researchers find that using microstimulation to impose a misfiring of relevant neurons for a memory task is unsuccessful in deteriorating task performance, presumably because there are compensatory mechanisms such as neuronal redundancy. This redundancy would give an immediate justification for the low-dimensionality of neural data.
3) **Neurons form common underlying networks.** Researchers have observed that in many cases the single-neuron firing patterns appear completely unrelated to externally measurable or controllable variables [5], and it is necessary to analyse populations of neurons. This observation, that neural data fundamentally cannot be understood on a single-neuron basis, yields the conclusion that neuron signals covary according to an underlying network, which might be parameterized by a much smaller number of variables than the number of neurons forming it. Thus, neural data should reside on lower-dimensional objects, such as manifolds.

We wish to note that aggressively pre-processing neural data is a common step in any dimension reduction pipeline in the neuroscience literature. One should be careful in correctly identifying that the low-dimensionality arises from the data rather than from the transformations applied to it. For example, if low-dimensionality only appears in a dataset after rejecting data sampled from a given electrode, it might be because the electrode was faulty and unreliable or because we introduced bias to the data. However, in most cases the pre-processing is physically meaningful and interpretable, so this concern can be neglected. A common and interpretable transformation which induces low-dimensionality is a time-frequency transformation, since neuron firing frequency changes may capture more information than the original time-domain data.

II. Computations and Visualizations for mc-1 dataset

For this project, we consider the mc-1 bilateral dataset for trial S6 (2018-10-04) from [7], which is available thanks to the CRCNS (Collaborative Research in Computational Neuroscience). This dataset corresponds to 64 electrodes recording neural activity in the motor cortex while a monkey gets food using both its left and right hands for about 12 minutes. The sampling frequency is 1kHz. The raw data for one channel is shown in Figure 3. First, we preprocess the data using the following pipeline:

1) We model each electrode's time signal with an auto regressive (AR) model.
2) We learn the AR model parameters ϕ_i using *modified covariance*.
3) We transform the data to a time-frequency space using an explicit transformation formula given the AR parameters.

4) We split the frequency space into 7 continuous bins, and we represent the frequency-domain content at each point in time with each bin's average.
5) We analyse the time-varying frequency average of each bin independently from the other bins.

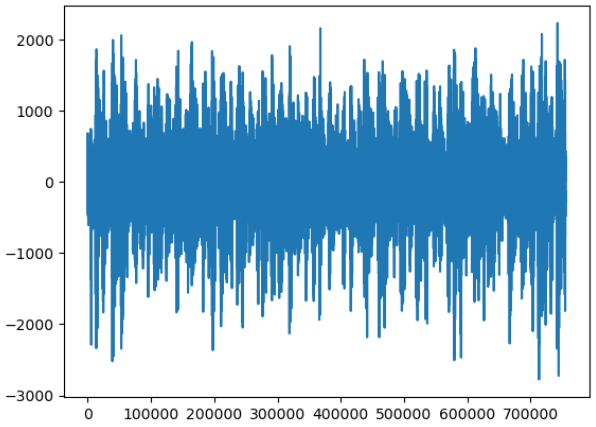

Fig. 3: This depicts the time-domain signal for one electrode in the mc-1 dataset.

A. Auto regressive model

The autoregressive model represents each point in a time signal as a weighted average of the preceding p samples, where p denotes the order of the model. In this case, we set $p = 20$. We have

$$x[n] = \sum_{i=1}^{p} \phi[i]x[n-i] + \varepsilon[n]$$

where $\phi[i]$ denote the weights of the AR model, $\varepsilon[n]$ denotes an error term which we attempt to minimize when learning ϕ, and $x[n]$ denotes a length-N signal (in our case, the time-domain neural data for one electrode). We learn ϕ using the modified covariance method:

$$\phi = \arg\min_{\phi' \in \mathbb{R}^p} \sum_{n=p+1}^{N} \left(x[n] - \sum_{k=1}^{p} \phi'[k]x[n-k] \right)^2 + \left(x[n-p] - \sum_{k=1}^{p} \phi'[k]x[n-p+k] \right)^2$$

This minimizes the sum of the *forward* (left term) and *backward* (right term) least-squares error. There's a nice trick to solve this explicitly: we can write these expressions as matrices. We write

$$\mathbf{X}_f = \begin{bmatrix} x[p] & x[p-1] & \dots & x[1] \\ x[p+1] & x[p] & \dots & x[2] \\ \vdots & \vdots & & \vdots \\ x[N-1] & x[N-2] & \dots & x[N-p] \end{bmatrix}$$

and

$$\mathbf{X}_b = \begin{bmatrix} x[1] & x[2] & \dots & x[p] \\ x[2] & x[3] & \dots & x[p+1] \\ \vdots & \vdots & & \vdots \\ x[N-p] & x[N-(p-1)] & \dots & x[N] \end{bmatrix}$$

Then, we rewrite the minimization problem as

$$\phi = \arg\min_{\phi'} ||\mathbf{x}_f - \mathbf{X}_f\phi'||^2 + ||\mathbf{x}_b - \mathbf{X}_b\phi'||^2$$

where $\mathbf{x}_f, \mathbf{x}_b \in \mathbb{R}^{N-p}$ are the first and last $N-p$ entries of the signal $x[n]$, respectively.
Finally, writing

$$\mathbf{X} = \begin{bmatrix} \mathbf{X_f} \\ \mathbf{X_b} \end{bmatrix}$$

and

$$\mathbf{x} = \begin{bmatrix} \mathbf{x}_f \\ \mathbf{x}_b \end{bmatrix}$$

we have

$$\phi = \arg\min_{\phi'} ||\mathbf{x} - \mathbf{X}\phi'||^2$$

which yields the explicit solution:

$$\boxed{\phi = (\mathbf{X}^T\mathbf{X})^{-1}\mathbf{X}^T\mathbf{x}}$$

B. Time-Frequency Representation

Now, we wish to model how the neuron firing frequency changes over time. To do this, we window the time signal with a 1 second window (corresponding to 1000 samples) and a 100ms time step (corresponding to 100 samples) and we fit an order-20 AR model to each window. We recall that the AR model has an explicit frequency domain representation:

$$P(f) = \frac{\hat{\sigma}^2}{|1 - \sum_{k=1}^{p} \phi[k] \exp(-j2\pi fk/f_s)|^2}$$

For each window, we bin the frequency domain into seven frequency bands:

- $\delta = [0.3\text{Hz}, 5\text{Hz}]$
- $\theta = [5\text{Hz}, 15\text{Hz}]$
- $\beta = [15\text{Hz}, 30\text{Hz}]$
- $\gamma_1 = [30\text{Hz}, 50\text{Hz}]$
- $\gamma_2 = [50\text{Hz}, 100\text{Hz}]$
- $\gamma_3 = [100\text{Hz}, 200\text{Hz}]$
- hfECoG $= [200\text{Hz}, 400\text{Hz}]$

and for we compute the average of each frequency band.

Thus, the output of our preprocessing has dimensions

$$7550 \text{ (\#windows)} \times 7 \text{ (\# freq. bins)} \times 64\text{(\# electrodes)}$$

and we treat each the time-varying average of each band as its own dataset. These are 7 different 64-dimensional datasets with 7550 samples.

C. Visualizations

We perform the following visualizations of the pre-processed data for various frequency bands:

1) 3-d visualizations of the data according to its top 3 principle components.
2) Scree plots for the principle component decay for subsets of data which satisfy $x \in B(x_k, R)$ for some randomly selected data point x_k and a reasonable value of R, averaged over 200 random selections of x_k.
3) 3-d visualizations of manifold traversal networks [19] which we learn from the data.
4) Isomap visualizations of the data, with the target dimension as $d = 2$, $d = 3$, and $d = 8$. For $d = 8$, we plot the top 3 principle components. Also, we show the scree plot for the $d = 8$ Isomap embedding.

These visualizations are shown in Figures 4, 5, 6, 7, 8, 9, 10 11, 12, and 13 respectively.

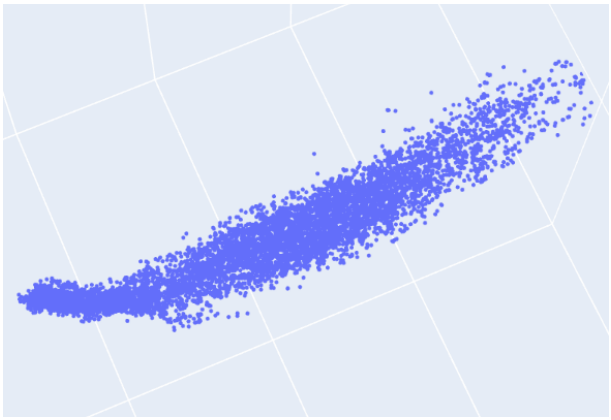

Fig. 4: This is a 2-d screenshot of the 3-d visualization of the top 3 principle components of the hfECoG dataset.

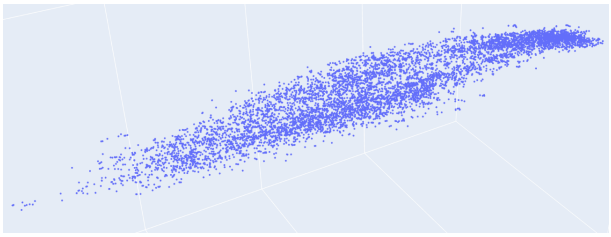

Fig. 5: This is a 2-d screenshot of the 3-d visualization of the top 3 principle components of the γ_3 dataset.

D. Discussion of Visualization Results

First, we note that all the axes are equally scaled for all 3-d visualizations. Clearly, there is some low-dimensionality to the data, as evidenced by the rapid principle component decay in the scree plots for local

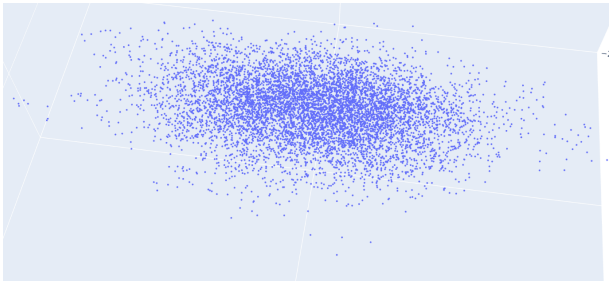

Fig. 6: This is a 2-d screenshot of the 3-d visualization of the top 3 principle components of the δ dataset.

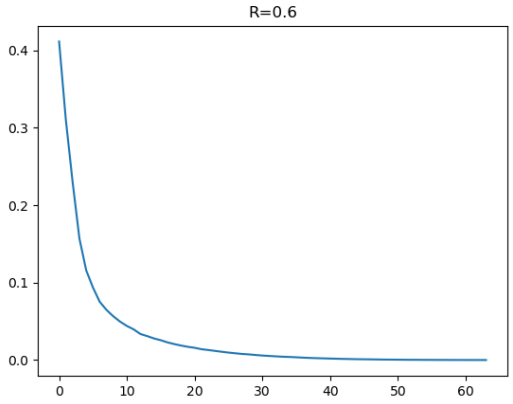

Fig. 7: This is the scree plot for the average principle component decay for subsets of neighboring datapoints in the hfECoG dataset, with the radius of the Euclidean ball $R = 0.6$.

data, and 3-d visualizations of the top 3 principle components of the hfECoG and γ_3 datasets, especially. We notice that the higher frequency datasets tend to exhibit more structure – the low-frequency δ dataset seems like a gaussian blob. Furthermore, we notice the uneven density: in the hfECoG and in the γ_3 datasets, there is a dense core from which emerges a sort of tail; this might be most obvious from the manifold traversal network image. From the Isomap embeddings, we notice that there is a curve in the dataset which the algorithm accentuates in both 2-d and 3-d. Nonetheless, the Isomap embedding fits pretty well to a single dimension: notice the scale discrepancy in Figure 11 and the sharp dropoff in the Scree plot for the 8-dimensional Isomap embedding in Figure 13. We are bothered that there is no sharp elbow in the scree plots in Figures 7, 8, and 9, but we understand that a well-defined, sharp elbow is uncommon in real datasets.

Due to severe time constraints, the authors were regrettably unable to produce similar visualizations for

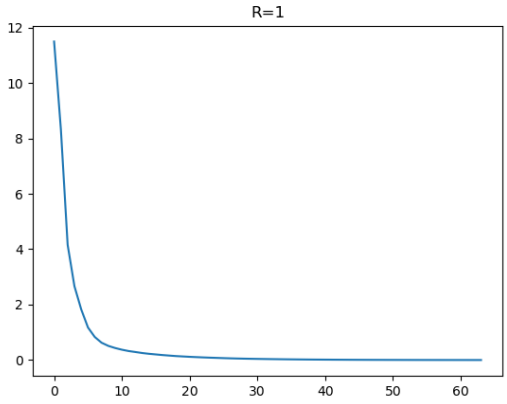

Fig. 8: This is the scree plot for the average principle component decay for subsets of neighboring datapoints in the γ_3 dataset, with the radius of the Euclidean ball $R = 1$.

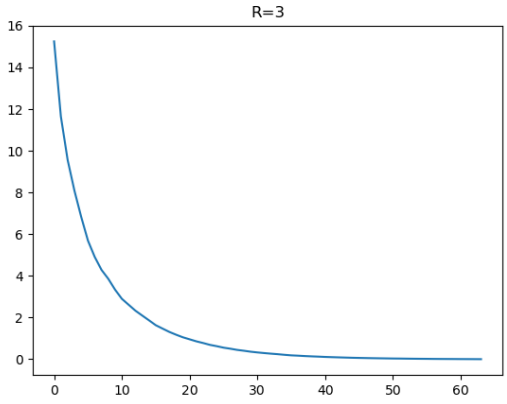

Fig. 9: This is the scree plot for the average principle component decay for subsets of neighboring datapoints in the δ dataset, with the radius of the Euclidean ball $R = 3$.

other datasets from mc-1 (such as the unilateral and ipsilateral experiments) or from other neuroscientific datasets, although we did play with the dataset produced from the experiments where a monkey controlled a cursor using a BCI from [6]. Although there are interesting ideas in the paper, we were unable to produce interesting results from the dataset. We elaborate on this in the following section. Lastly, we note that the mc-1 dataset (for this particular bilateral movement experiment) includes both the ECoG data and some data describing the hand positions as they change in time. In the dataset's original paper, the authors break the time series into sections corresponding to idle hands, right hand movement, and

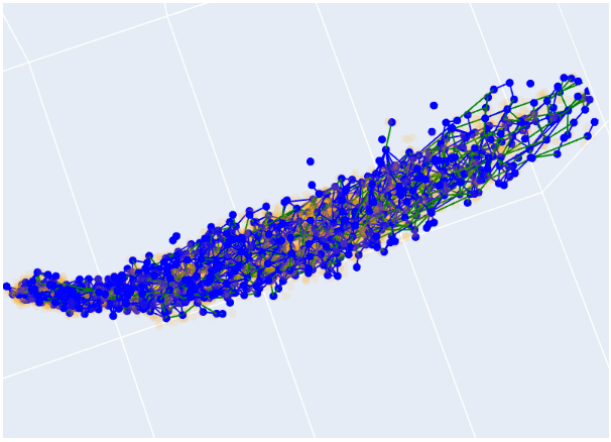

Fig. 10: This is a 2-d screenshot of the 3-d visualizzation of a manifold traversal network fit to the hfECoG data.

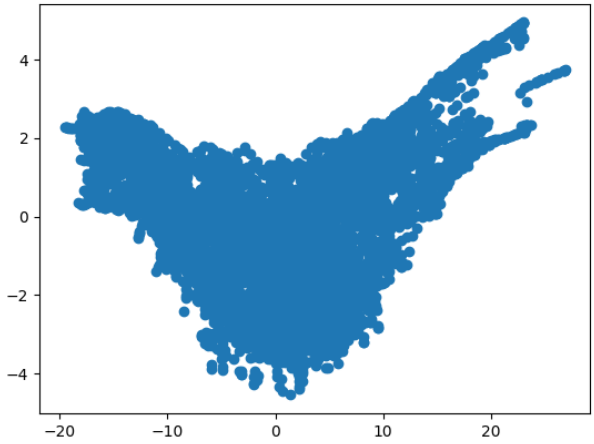

Fig. 11: This is a scatterplot for the 2-dimensional Isomap embedding of the hfECoG data.

left hand movement to ultimately perform supervised feature extraction. We wish to extract these labels and plot the labeled data to determine whether the these labels have geometric meaning.

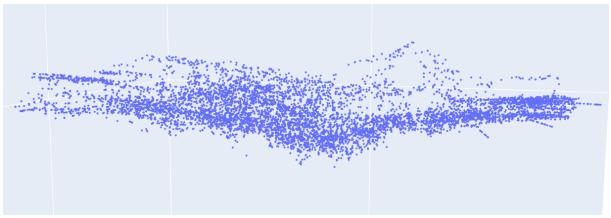

Fig. 12: This is a 2-d screenshot of the 3-dimensional Isomap embedding of the hfECoG data.

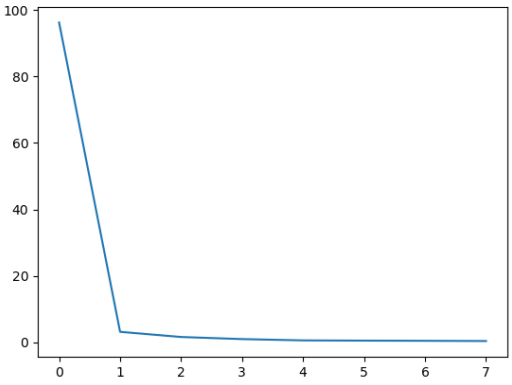

Fig. 13: This is a plot of the principle component decay of the 8-dimensional Isomap embedding of the hfECoG data.

III. Computations from cursor BCI dataset from [6]

The dataset from this paper is interesting because there is a clear problem which we aim to solve using data analysis. This dataset corresponds to experiments involving two monkeys using a BCI to control a cursor and move it to a target on a screen. The interesting aspect of the problem is that the dataset is broken into about 500 trials, each consisting of about 15 samples from their 96 electrode system. The overall goal is to relate each 96-dimensional time sample to a cursor velocity. As mentioned in the introduction, this is done by using a fixed Kalman filter. The paper seeks to improve performance in the prsence of recording instability by identifying deficient electrodes and ignoring them, and by leveraging assumptions about the low-dimensionality of the data to relate the data from different trials, which they call *stabilizing*. Specifically, there may be permutations, baseline shifts, and tuning changes in the electrodes which they wish to remove by assuming that the data from all trials belong to the same linear subspace (or "manifold", according to their work) and transforming the data from different trials so that they reside on the same linear subspace which they learn during a calibration phase. They do this in the following way:

1) Use factor analysis to extract a 10 dimensional latent state z_t from a 93 dimensional sample u_t (because they identify 3 electrodes as deficient), yielding $u_t|z_t \sim \mathcal{N}(\Lambda z_t + \mu, \Psi)$ where Λ is the loading matrix relating z_t to q_t.
2) Aligning the latent state to the baseline calibration by solving the Procrustes problem:
$$\hat{O} = \underset{O:OO^T=I}{\arg\min} \left|\left|\Lambda_1 - \Lambda_2 O^T\right|\right|_F^2$$
where Λ_1 will be learned during calibration, and Λ is the loading matrix for the factor analysis of that time sample. From this, produce $\tilde{\Lambda} = \Lambda_2 O^T$.
3) Stabilize the estimate of the latent state with
$$\tilde{z}_t = \beta(u_t - \mu)$$
where $\beta = \tilde{\Lambda}^T(\tilde{\Lambda}\tilde{\Lambda}^T + \Psi)^{-1}$.

The author learned a few things from this pipeline: first, factor analysis fits a linear subspace (like PCA) but tries to spread the variance of the latent state equally in all of its embedding dimensions. Factor analysis has that $z_t \sim \mathcal{N}(0, I_{10})$. The factor analysis parameters are learned using expectation maximization. Then, the Procrustes problem is satisfying because it yields an elegant closed-form solution:

$$O^\star = VU^T \text{ for } U\Sigma V^* = (\Lambda_2^T \Lambda_1)$$

. The proof for this closed-form solution is also satisfying.

We were unable to produce nice results from the dataset; perhaps the issue arises from mistakes in the our code. Nonetheless, there is something surprising about fitting a 10 dimensional subspace to 15 data points.

IV. Discussion

In neuroscience research, the specific properties of the low-dimensional object are not known. Does neural data reside on a Riemannian manifold? How much progress can be made by fitting low-dimensional linear subspaces to neural data? Is the object under consideration more complicated than a fixed manifold? While this last question is certainly speculative, there are some fun ideas in the space regarding this. For example, the manifold on which neural data resides might change as new neural pathways are created – the brain is likely not a static system, but rather one that evolves. It seems reasonable to expect that the neural manifolds for two distinct adults may be different, so it seems reasonable to expect that the neural manifolds for the same person might be different at different stages in their life. So, how fast might a neural manifold change, and how might one model a changing manifold?

Otherwise, there is a new, famous dataset which has yielded some interesting observations. This dataset consists of calcium imaging of a larval zebrafish's neural activity [1], and the observation is that different subsets of the neural data yield low-dimensional structures in isolation, but not jointly. An incredibly aggressive hypothesis by this author is that neural data may exhibit multiple manifold-like structures which might interact in some fashion. For example, supposing that neural data from the visual cortex and motor cortex both satisfied

the manifold hypothesis and that these two sections of the brain were fully independent, then a neural dataset consisting of neurons from both regions would exhibit a structure corresponding to two orthogonal manifolds! For future work, we are curious to explore this zebrafish dataset because of its incredible size (1TB / hour!) and the ability to examine the relationship between low-dimensionality between sets of neurons and their location on the zebrafish's brain.

Note: we include the entire bibliography produced by this author's Zotero, so some papers in the section are not cited in this write-up but were considered by this author.

References

[1] Misha B. Ahrens et al. "Brain-wide neuronal dynamics during motor adaptation in zebrafish". en. In: *Nature* 485.7399 (May 2012). Publisher: Nature Publishing Group, pp. 471–477. ISSN: 1476-4687. DOI: 10.1038/nature11057. URL: https://www.nature.com/articles/nature11057 (visited on 05/16/2025).

[2] Misha B. Ahrens et al. "Whole-brain functional imaging at cellular resolution using light-sheet microscopy". en. In: *Nature Methods* 10.5 (May 2013). Publisher: Nature Publishing Group, pp. 413–420. ISSN: 1548-7105. DOI: 10.1038/nmeth.2434. URL: https://www.nature.com/articles/nmeth.2434 (visited on 05/15/2025).

[3] Jiaming Cao and Pulkit Grover. "STIMULUS: Noninvasive Dynamic Patterns of Neurostimulation Using Spatio-Temporal Interference". In: *IEEE Transactions on Biomedical Engineering* 67.3 (Mar. 2020), pp. 726–737. ISSN: 1558-2531. DOI: 10.1109/TBME.2019.2919912. URL: https://ieeexplore.ieee.org/document/8726149 (visited on 05/15/2025).

[4] Mark M. Churchland et al. "Neural population dynamics during reaching". en. In: *Nature* 487.7405 (July 2012). Publisher: Nature Publishing Group, pp. 51–56. ISSN: 1476-4687. DOI: 10.1038/nature11129. URL: https://www.nature.com/articles/nature11129 (visited on 05/15/2025).

[5] John P. Cunningham and Byron M. Yu. "Dimensionality reduction for large-scale neural recordings". en. In: *Nature Neuroscience* 17.11 (Nov. 2014). Publisher: Nature Publishing Group, pp. 1500–1509. ISSN: 1546-1726. DOI: 10.1038/nn.3776. URL: https://www.nature.com/articles/nn.3776 (visited on 05/15/2025).

[6] Alan D. Degenhart et al. "Stabilization of a brain–computer interface via the alignment of low-dimensional spaces of neural activity". en. In: *Nature Biomedical Engineering* 4.7 (July 2020). Publisher: Nature Publishing Group, pp. 672–685. ISSN: 2157-846X. DOI: 10.1038/s41551-020-0542-9. URL: https://www.nature.com/articles/s41551-020-0542-9 (visited on 05/15/2025).

[7] Behraz Farrokhi and Abbas Erfanian. "A state-based probabilistic method for decoding hand position during movement from ECoG signals in non-human primate". en. In: *Journal of Neural Engineering* 17.2 (May 2020). Publisher: IOP Publishing, p. 026042. ISSN: 1741-2552. DOI: 10.1088/1741-2552/ab848b. URL: https://dx.doi.org/10.1088/1741-2552/ab848b (visited on 05/15/2025).

[8] Jay A Hennig et al. "Constraints on neural redundancy". In: *eLife* 7 (Aug. 2018). Ed. by Eric Shea-Brown and Timothy E Behrens. Publisher: eLife Sciences Publications, Ltd, e36774. ISSN: 2050-084X. DOI: 10.7554/eLife.36774. URL: https://doi.org/10.7554/eLife.36774 (visited on 05/15/2025).

[9] Kejia Hu et al. "Decoding unconstrained arm movements in primates using high-density electrocorticography signals for brain-machine interface use". en. In: *Scientific Reports* 8.1 (July 2018). Publisher: Nature Publishing Group, p. 10583. ISSN: 2045-2322. DOI: 10.1038/s41598-018-28940-7. URL: https://www.nature.com/articles/s41598-018-28940-7 (visited on 05/15/2025).

[10] Takashi Kawashima et al. "The Serotonergic System Tracks the Outcomes of Actions to Mediate Short-Term Motor Learning". English. In: *Cell* 167.4 (Nov. 2016). Publisher: Elsevier, 933–946.e20. ISSN: 0092-8674, 1097-4172. DOI: 10.1016/j.cell.2016.09.055. URL: https://www.cell.com/cell/abstract/S0092-8674(16)31379-4 (visited on 03/13/2025).

[11] Tze Hui Koh et al. "Dimensionality reduction of calcium-imaged neuronal population activity". en. In: *Nature Computational Science* 3.1 (Dec. 2022), pp. 71–85. ISSN: 2662-8457. DOI: 10.1038/s43588-022-00390-2. URL: https://www.nature.com/articles/s43588-022-00390-2 (visited on 03/13/2025).

[12] J. A. Menéndez et al. *A theory of brain-computer interface learning via low-dimensional control*. en. Apr. 2024. DOI: 10.1101/2024.04.18.589952. URL: http://biorxiv.org/lookup/doi/10.1101/2024.04.18.589952 (visited on 03/13/2025).

[13] J. A. Menéndez et al. *A theory of brain-computer interface learning via low-dimensional control*. en. Pages: 2024.04.18.589952 Section: New Re-

sults. Apr. 2024. DOI: 10.1101/2024.04.18.589952. URL: https://www.biorxiv.org/content/10.1101/2024.04.18.589952v1 (visited on 05/15/2025).

[14] Emily R. Oby et al. "Dynamical constraints on neural population activity". en. In: *Nature Neuroscience* 28.2 (Feb. 2025). Publisher: Nature Publishing Group, pp. 383–393. ISSN: 1546-1726. DOI: 10.1038/s41593-024-01845-7. URL: https://www.nature.com/articles/s41593-024-01845-7 (visited on 05/15/2025).

[15] Joana Soldado-Magraner et al. *Robustness of working memory to prefrontal cortex microstimulation*. en. Pages: 2025.01.14.632986 Section: New Results. Jan. 2025. DOI: 10.1101/2025.01.14.632986. URL: https://www.biorxiv.org/content/10.1101/2025.01.14.632986v1 (visited on 03/13/2025).

[16] Joana Soldado-Magraner et al. *Robustness of working memory to prefrontal cortex microstimulation*. en. Jan. 2025. DOI: 10.1101/2025.01.14.632986. URL: http://biorxiv.org/lookup/doi/10.1101/2025.01.14.632986 (visited on 05/15/2025).

[17] Akash Umakantha et al. "Bridging neuronal correlations and dimensionality reduction". In: *Neuron* 109.17 (2021). Publisher: Elsevier, pp. 2740–2754. URL: https://www.cell.com/neuron/fulltext/S0896-6273(21)00469-4 (visited on 03/13/2025).

[18] Praveen Venkatesh, Sanghamitra Dutta, and Pulkit Grover. *Information Flow in Computational Systems*. Feb. 2019. DOI: 10.48550/arXiv.1902.02292.

[19] Shiyu Wang et al. *Fast, Accurate Manifold Denoising by Tunneling Riemannian Optimization*. en. arXiv:2502.16819 [cs]. Feb. 2025. DOI: 10.48550/arXiv.2502.16819. URL: http://arxiv.org/abs/2502.16819 (visited on 03/13/2025).